Monthly Notices
of the
ROYAL ASTRONOMICAL SOCIETY

MNRAS **432,** 285–300 (2013)
Advance Access publication 2013 April 10

doi:10.1093/mnras/stt459

# The spatial extent and distribution of star formation in 3D-*HST* mergers at $z \sim 1.5$

Kasper B. Schmidt,[1,2⋆] Hans-Walter Rix,[1] Elisabete da Cunha,[1] Gabriel B. Brammer,[3] Thomas J. Cox,[4] Pieter van Dokkum,[5] Natascha M. Förster Schreiber,[6] Marijn Franx,[7] Mattia Fumagalli,[7] Patrik Jonsson,[8] Britt Lundgren,[5] Michael V. Maseda,[1] Ivelina Momcheva,[5] Erica J. Nelson,[5] Rosalind E. Skelton,[5] Arjen van der Wel[1] and Katherine E. Whitaker[9]

[1]*Max Planck Institut für Astronomie, Königstuhl 17, D-69117 Heidelberg, Germany*
[2]*Department of Physics, University of California, Santa Barbara, CA 93106, USA*
[3]*European Southern Observatory, Alonso de Córdova 3107, Casilla 19001, Vitacura, Santiago, Chile*
[4]*Carnegie Observatories, 813 Santa Barbara Street, Pasadena, CA 91101, USA*
[5]*Department of Astronomy, Yale University, New Haven, CT 06520, USA*
[6]*Max Planck Institut für Extraterrestrische Physik, Giessenbachstrasse, D-85748 Garching, Germany*
[7]*Leiden Observatory, Leiden University, PO Box 9513, Leiden, RA 2300, the Netherlands*
[8]*Harvard-Smithsonian Center for Astrophysics, 60 Garden Street, Cambridge, MA 02138, USA*
[9]*Astrophysics Science Division, Goddard Space Flight Center, Code 665, Greenbelt, MD 20771, USA*

Accepted 2013 March 13. Received 2013 February 28; in original form 2012 September 23

## ABSTRACT

We present an analysis of the spatial distribution of star formation in a sample of 60 visually identified galaxy merger candidates at $z > 1$. Our sample, drawn from the 3D-*HST* survey, is flux limited and was selected to have high star formation rates based on fits of their broad-band, low spatial resolution spectral energy distributions. It includes plausible pre-merger (close pairs) and post-merger (single objects with tidal features) systems, with total stellar masses and star formation rates derived from multiwavelength photometry. Here we use near-infrared slitless spectra from 3D-*HST* which produce H$\alpha$ or [O III] emission line maps as proxies for star formation maps. This provides a first comprehensive high-resolution, empirical picture of *where* star formation occurred in galaxy mergers at the epoch of peak cosmic star formation rate. We find that detectable star formation can occur in one or both galaxy centres, or in tidal tails. The most common case (58 per cent) is that star formation is largely concentrated in a single, compact region, coincident with the centre of (one of) the merger components. No correlations between star formation morphology and redshift, total stellar mass or star formation rate are found. A restricted set of hydrodynamical merger simulations between similarly massive and gas-rich objects implies that star formation should be detectable in both merger components, when the gas fractions of the individual components are the same. This suggests that $z \sim 1.5$ mergers typically occur between galaxies whose gas fractions, masses and/or star formation rates are distinctly different from one another.

**Key words:** galaxies: formation – galaxies: interactions – galaxies: starburst – galaxies: structure.

## 1 INTRODUCTION

The spatial extent and distribution of star formation in normal, local galaxies is well established (e.g. James et al. 2004; Bigiel et al. 2008; Bigiel, Leroy & Walter 2011; Schruba et al. 2011; Calzetti, Liu & Koda 2012, and references therein). Both self-regulated star formation and merging must be key ingredients in galaxy formation and evolution and have been studied observationally in detail in the $z \lesssim 0.5$ Universe (e.g. Barton, Geller & Kenyon 2000; Lambas et al. 2003; Hammer et al. 2005; Barton et al. 2007; Jogee et al. 2009; Robaina et al. 2009, 2010) as well as in theoretical simulations

⋆E-mail: kschmidt@physics.ucsb.edu

(e.g. Barnes & Hernquist 1996; Mihos & Hernquist 1996; Springel 2000; Cox 2004; Cox et al. 2006, 2008; di Matteo et al. 2007; Lotz et al. 2008a,b). From these studies, it has become evident that rapid star formation can be triggered by tidal interaction in mergers, but the simulations also suggest that mergers trigger both nuclear starbursts and black hole accretion. Even though galaxy mergers are observed to enhance star formation in galaxies and trigger some of the most violent starbursts known (e.g. Joseph & Wright 1985; Rieke et al. 1985; Melnick & Mirabel 1990; Klaas & Elsaesser 1991), it appears that the net effect of major mergers in the global star formation history of the galaxy population has been relatively modest since at least $z = 1$ (e.g. Jogee et al. 2009; Robaina et al. 2009).

Mergers are predicted to play a crucial role in the build-up and formation of massive galaxies (e.g. Mihos & Hernquist 1996; Springel 2000; Cox et al. 2008; Hopkins et al. 2010), and therefore, a crucial step towards fully understanding how galaxies have evolved is to study the star formation properties in merging systems at high redshifts. Some of the questions that need to be addressed observationally to get a more detailed picture of the star formation history of present-day galaxies are the following: Where did stars form in merging galaxies at higher redshift? and Which phase(s) of the merging process seems to trigger most star formation?

At higher redshift, the interplay between merging and star formation has been investigated in much less detail than in the local Universe. This is mostly due to observational challenges, as resolved observations at <1 arcsec resolution are needed. Further, tracing star formation e.g. through H$\alpha$ at $z \sim 1.5$ requires observations in the near-infrared (NIR), and these have been far less feasible than observations in optical wavebands. Nevertheless, the $0.7 < z < 2$ epoch is immensely important for understanding galaxy formation, as this is the cosmic time when the majority of the stars we see in galaxies today were formed (e.g. Hopkins & Beacom 2006; Karim et al. 2011). Several studies have addressed the impact of (major) galaxy mergers as well as the general galaxy morphology on the amount of star formation at $z \sim 1.5$ (e.g. Swinbank et al. 2004; Law et al. 2007; Förster Schreiber et al. 2009; Wright et al. 2009; Conselice et al. 2011; Bell et al. 2012; Bluck et al. 2012). However, only a few of these studies investigate three-dimensional (3D) spectroscopy, where both spatial and spectral information is available, which is crucial for investigating the *spatial* extent of star formation.

Until recently, large samples of galaxies, and in particular galaxy mergers, with rest-frame optical 3D spectroscopic information at high redshift did not exist. The largest samples of galaxies with such data at $1.5 < z < 2.5$ are from the Spectroscopic Imaging survey in the Near-infrared with SINFONI (SINS; Förster Schreiber et al. 2009), recently expanded with the zCOSMOS (zC)-SINF sample (Mancini et al. 2011), totalling 110 star-forming galaxies at $1.5 \lesssim z \lesssim 2.5$ observed with Spectrograph for Integral Field Observation in the Near Infrared (SINFONI), and from the Mass Assembly Survey with SINFONI in VVDS (MASSIV; Contini et al. 2012) which contains 84 star-forming galaxies at $0.9 < z < 1.8$ also mapped with SINFONI. Using H$\alpha$ as kinematic and star formation tracer enabled analysis of the spatially resolved ionized gas kinematics, its distribution and the physical properties of these systems (Genzel et al. 2006, 2008, 2011; Shapiro et al. 2008; Cresci et al. 2009; Epinat et al. 2009, 2012; Queyrel et al. 2009, 2012; Newman et al. 2012). High-resolution NIR imaging with the *Hubble Space Telescope* (*HST*) Near Infrared Camera and Multi-Object Spectrometer 2 (NICMOS2) for a small subset of the SINS objects provided additional rest-frame optical morphologies, in agreement with the disc or merger nature from the H$\alpha$ kinematics (Förster Schreiber et al. 2011a,b). The selection of these samples was primarily based on integrated photometry or spectroscopic properties, not morphologies, and only a modest fraction of objects ($\sim$1/3) were kinematically inferred to be (major) mergers. Roughly comparable fractions were found in other sizeable NIR integral field unit (IFU) samples at $z \sim 1$–3, including e.g. those by Law et al. (2007, 2009), Gnerucci et al. (2011) and Wisnioski et al. (2011b).

With the recent 3D-*HST* slitless grism survey (see Brammer et al. 2012, and Section 2), much larger samples of objects with NIR 3D emission line spectroscopy have become available, making it possible to address the spatial extent of star formation for extensive samples of galaxy mergers at the peak of cosmic star formation rate (SFR) density. The IFU samples mentioned above have significantly higher spectral resolution, enabling detailed kinematic studies, but adaptive optics (AO)-assisted IFU observations, which provide angular resolution comparable to *HST* in the NIR, remain observationally expensive and suffer from complications due to strong night sky lines. *HST* grism observations, as the ones taken in the 3D-*HST* survey, provide more limited kinematic information but allow for unbiased target selection and are much more efficient at detecting and mapping the continuum and line emission at high angular resolution for all targets within the field-of-view. 3D-*HST* provides resolved line emission, enabling studies of the spatial extent of star formation for large samples of galaxies at $z > 1$ in five well-studied cosmological fields. The initial papers use approximately half of the full data set, as described in van Dokkum et al. (2011) and Brammer et al. (2012).

Using the same 3D-*HST* data, we explore the spatial extent and distribution of star formation in a 'population snapshot' of presumably *merging* systems at $z \sim 1.5$. For this sample we make $\sim$0.2 arcsec resolution maps of emission lines (H$\alpha$ and [O III]), which trace the spatial extent of the (unobscured) star formation in these mergers and allow us to study their star formation properties in a statistical and unbiased way. This is done under the assumption that the H$\alpha$ (for $z \sim 0.7$–1.5) and [O III] (for $z \sim 1.2$–2.3) emission of the systems trace the star formation. This has been shown to be a fair assumption for both H$\alpha$ (Kennicutt 1983, 1998a,b; Gallagher, Hunter & Tutukov 1984; Kennicutt, Tamblyn & Congdon 1994) and [O III] (Kennicutt 1992; Teplitz et al. 2000; Hippelein et al. 2003), even though using [O III] as a quantitative indicator of SFR (which is not what we aim to do here) includes several complicating factors (Teplitz et al. 2000).

To help interpret our observations in a theoretical context, we create a sample of pseudo-observations from state-of-the-art smoothed particle hydrodynamic (SPH) simulations of individual mergers, which we compare to the 3D-*HST* data. The simulations predict a merger sequence and star formation picture with centrally concentrated triggered starbursts at final coalescence, enhanced star formation in tidal features, and black hole growth and accretion. The goal is to understand the observational results from 3D-*HST* by making a direct comparison with the predictions from the simulations. These comparisons will help explore which parameters, e.g. viewing angle, merger phase, gas fraction, mass ratio etc., play a crucial role in determining, for example, SFRs from observations.

In Section 2 we describe the 3D-*HST* survey from which the merger sample was selected. We then describe the selection of our sample in Section 3 and the procedure used to map the spatial extent of the star formation in Section 4. In Section 5 we split the sample into four different morphological types and find that most mergers exhibit star formation in only one component. In Section 6 we compare numerical merger simulations to the observed 3D-*HST*

spectra and find that in simulations star formation most commonly occurs in both components, before we summarize and conclude in Section 7.

## 2 THE 3D-*HST* SURVEY DATA

To construct the 0.2 arcsec resolution emission line maps, the proxies for star formation maps, we take advantage of the NIR 3D spectroscopy survey possibilities that the Wide Field Camera 3 (WFC3) on *HST* brings. The 3D-*HST* survey is a 248 orbit NIR spectroscopic Hubble treasury program (Cycles 18 and 19, PI: van Dokkum). It provides NIR imaging with the *F140W* filter and grism spectroscopy with the G141 grism over well-studied extragalactic survey fields [All-Wavelength Extended Groth Strip International Survey (AEGIS), Cosmic Evolution Survey (COSMOS), Great Observatories Origins Deep Survey-South (GOODS-S), Great Observatories Origins Deep Survey-North (GOODS-N) and UKIRT Infrared Deep Sky Survey (UKIDSS)/Ultra Deep Survey (UDS)]. The grism spectroscopy is slitless so both spatial and spectroscopic information is available for every single object in the survey fields. The 3D-*HST* survey provides rest-frame optical spectra for a sample of ∼7000 galaxies at $1 < z < 3.5$ (van Dokkum et al. 2011; Brammer et al. 2012).

As of 2011 August the survey had observed 68 pointings over the GOODS-S, GOODS-N,[1] COSMOS and AEGIS fields (van Dokkum et al. 2011). The present work is based on 30 of these 68 pointings, where the extensive ancillary data available enables robust spectral energy distribution (SED) modelling necessary for our sample selection as described in Section 3.

### 2.1 The 3D-*HST* grism spectroscopy

The WFC3 G141 grism used in 3D-*HST* disperses the light over the wavelength range from 1.05 to 1.7 μm with a low spectral resolution of $R \sim 130$.

Since the grism spectroscopy is slitless, the WFC3 G141 grism basically produces an emission line image that is superimposed on to a sequence of dispersed monochromatic continuum images, and some of the key features of slitless spectroscopy therefore need to be taken into account. First of all, the width of emission/absorption lines in the dispersion direction in slitless spectroscopy is not only caused by velocity broadening (which is negligible for the low-resolution 3D-*HST* spectra) and the intrinsic broadening of the wavelength dispersion: as slitless spectroscopy produces shifted monochromatic images, the spatial extent of the dispersed emission line image reflects the spatial distribution of the line emission both along and perpendicular to the dispersion direction. We will take advantage of this 'morphology broadening' (which can be seen in the third panel of Fig. 4) to map the spatial extent of star formation as described in Section 4. Fig. 4 will be explained in more detail here.

As with multislit spectroscopy, the differing wavelength coverage of the spectra is an issue. Since the detector on to which the field-of-view is dispersed has a finite size, approximately 10 per cent of the spectra are cut off on the edge of the detector.

Lastly, 'contamination' is an important property of slitless spectroscopy. Since the focal plane is not blocked out with a slit or a mask as is usually done in standard spectroscopy, all the light from a given object, and all other objects in the observed field, are dispersed on to the detector. Hence, spectra will often overlap and therefore 'contaminate' each other as explained in Brammer et al. (2012).

For more information on the data reduction methods, the data products of the 3D-*HST* survey and the survey itself, we refer to Brammer et al. (2012).

[1] The GOODS-N data were taken as part of the *HST* program GO-11600 (PI: B. Weiner).

## 3 SELECTING MERGER CANDIDATES

We select our sample of merger candidates from the first 68 pointings obtained as part of the 3D-*HST* survey based on three different inputs: (i) the 3D-*HST* survey catalogue, (ii) SED modelling and most importantly (iii) visual inspection of NIR (*F140W*) morphologies. The first two selection steps are performed to define an initial sample of systems with sufficient spectral coverage and to minimize the number of objects to visually inspect. We will describe each of these three steps below.

To obtain robust SFR estimates via the SED fitting described in Section 3.2, we require extensive ancillary photometric catalogues. We therefore focus on the 30 pointings of data available in GOODS-S (6) and COSMOS (24), where the photometric data in the FIREWORKS (Wuyts et al. 2008) and the NEWFIRM Medium Band Survey (NMBS; Whitaker et al. 2011) catalogues are available, respectively. Hence, this work is performed on approximately 1/5 of the final 3D-*HST* data product.

### 3.1 Grism catalogue cuts

The first step in defining our merger sample is to select a well-defined sample of objects based on the data products of the 3D-*HST* survey. We ensure that at least 75 per cent of each spectrum in the sample falls on the detector. Since we are looking for merging objects we do not put any constraints on the contamination of the individual spectra, as spectra of close pairs will always have a high level of contamination. We rely on the visual inspection (Section 3.3) to remove cases with heavy contamination from objects that are not part of the potentially merging system.

Each individual object in the 3D-*HST* catalogue has been matched to the available ancillary photometric catalogues. Since the 3D-*HST* catalogue is selected from the deep ($H_{F140W} \approx 26.1$; Brammer et al. 2012) high-resolution NIR *HST F140W* images, and the photometric catalogues are ground based and shallower, not all 3D-*HST* objects can be matched to an object in the photometric catalogues. We only selected objects with a counterpart (within 0.3 arcsec) in ground-based photometric catalogues. Faint objects have the risk of being assigned to a bright(er) counterpart's photometry, have low signal-to-noise ratio (S/N) and less reliable redshifts, and we therefore restrict ourselves to objects with $m_{F140W} \leq 23.5$.

Last but not least, the 3D-*HST* catalogues provide a redshift estimate for the objects based on the extracted grism spectra. The catalogue grism redshifts, $z_{\rm grism}$, are obtained by collapsing the 2D grism spectrum into a 1D spectrum, combining it with available photometry, and then estimating the redshift with an updated version of the EAZY code (Brammer, van Dokkum & Coppi 2008). The redshift range where H$\alpha$ and/or [O III] emission fall in the G141 grism wavelength range is $0.7 < z < 2.3$ (see fig. 1 in Brammer et al. 2012). We are interested in tracing the star formation in the merging systems via either H$\alpha$ or [O III] emission, and therefore use $z_{\rm grism}$ to select objects in this particular redshift range.

**Table 1.** Grism (top) and SED (bottom) selection criteria.

| | | | | |
|---|---|---|---|---|
| 0.75 | ≤ | Spectral coverage | | |
| | | Photometric match | ≤ | 0.3 arcsec |
| | | $m_{F140W}$ | ≤ | 23.5 |
| 0.7 | ≤ | $z_{\rm grism}$ | ≤ | 2.3 |
| 9.0 | ≤ | $\log\left(\frac{M_*}{[\mathrm{M}_\odot]}\right)$ | ≤ | 12.0 |
| −9.5 | ≤ | $\log\left(\frac{\mathrm{sSFR}}{[\mathrm{yr}^{-1}]}\right)$ | | |
| 1.0 | ≤ | $\log\left(\frac{\mathrm{SFR}}{[\mathrm{M}_\odot\,\mathrm{yr}^{-1}]}\right)$ | | |

Applying these five initial cuts (listed in the top half of Table 1) reduces the full sample of 21 460 detections in the 30 GOODS-S and COSMOS pointings to 1542 objects.

### 3.2 Fitting SEDs to photometry

We select star-forming systems that are expected to have significant emission line features based on their SFRs, specific SFR (sSFR) and stellar masses ($M_*$). We obtain the SFR, sSFR and $M_*$ of each individual object from modelling the SED based on the ancillary photometric catalogues using a Chabrier (2003) initial mass function (IMF) with the code MAGPHYS presented in da Cunha et al. (2008). We use the 37 NMBS bands (Whitaker et al. 2011) for the COSMOS objects and the 17 FIREWORKS bands (Wuyts et al. 2008) for the GOODS-S objects. Both catalogues span from the far-UV to Multiband Imaging Photometer for *Spitzer* (MIPS) 24 μm. The 3D-*HST* catalogue redshift $z_{\rm grism}$ is used as a prior when fitting the ancillary photometric data for each object.

Although the photometric measurements are a blend of two or more components in many cases, i.e. only one photometric ID corresponds to each merger whereas several components are clearly distinguishable in the high-resolution *HST* imaging, selecting the high-SFR objects based on SED fits to the photometry is still very effective in selecting objects with strong emission line features.

As shown in the bottom part of Table 1 we select objects with $\mathrm{SFR} > 10\,\mathrm{M}_\odot\,\mathrm{yr}^{-1}$, $\mathrm{sSFR} > 10^{-9.5}\,\mathrm{yr}^{-1}$ and $10^9 < M_* < 10^{12}\,\mathrm{M}_\odot$. A SFR of $10\,\mathrm{M}_\odot\,\mathrm{yr}^{-1}$ roughly corresponds to an emission line flux $F_{\mathrm{H}\alpha} \sim 10^{-16}$ erg s$^{-1}$ cm$^{-2}$ at $z = 1.5$ which corresponds to a (collapsed) emission line S/N of ∼8 at $1 \times 10^{-16}$ erg s$^{-1}$ cm$^{-2}$ (Brammer et al. 2012). Hence, concentrated star formation, i.e. emitted from a modest amount of pixels of this order, should be well detected in the 3D-*HST* spectra. On the other hand, if the total emission line flux $F_{\mathrm{H}\alpha}$ is spread over a larger area, the S/N per pixel might become too low for clear detection (see Section 5).

We find 352 of the initial 1542 objects in the $0.7 < z < 2.3$ range that satisfy these SED criteria.

### 3.3 Visual inspection of NIR morphology

Previous studies have argued both for visual (Robaina et al. 2009) and algorithmic merger identification (e.g. Conselice, Rajgor & Myers 2008; Lotz et al. 2008a). For this pilot study, which is focused on the *emission line morphology* not on the merger rates, we have, as discussed below, decided to use a visual classification. The visual inspection of the remaining 352 objects is the crucial final step in the merger sample selection process.

The visual inspection is based on the NIR *F140W* morphology of the objects from the 3D-*HST* direct imaging. The NIR images show the rest-frame optical emission at the redshifts of our galaxies. We assume that the observed NIR (i.e. rest-frame optical) morphology traces the distribution of the (intermediate-age) stellar component of the galaxies, and that it is therefore different from the stars being formed (current star formation) as traced by the emission lines. A caveat to such an assumption is that if a galaxy does not have a dominating intermediate-age stellar population and has a high SFR, the morphology in the rest-frame optical will to some extent reflect the distribution of young stars as well. The criteria used to select the merger candidates from the 352 objects are that (i) they should show a morphology that differs from the bulk of the 'normal' isolated galaxies, i.e. a disturbed irregular/asymmetric morphology, and (ii) they have to show several distinct components in the continuum image, either multiple objects within the ∼3 × 3 arcsec$^2$ *F140W* thumbnails or pronounced tidal features extending from the main continuum emission component. It should be noted that because our merger selection is based only on this visual classification, and the low resolution of the G141 grism ($R \sim 130$) does not offer any kinematic information of the individual companions, it is impossible to address whether or not the systems are gravitationally bound. Our merger sample therefore consists of *potentially* merging systems.

A fraction of the more widely separated merger pairs could therefore be potential low- or high-redshift interlopers which would artificially enhance the number of mergers found. The distances between the majority of the individual merger components in the candidates selected here are of the order 1 arcsec, corresponding to roughly 8.5 kpc at $z \sim 1.5$. Law et al. (2012) estimated that $7^{+1}_{-1}$ per cent of galaxies have projected false pairs within 16 kpc. This serves as an upper limit on the expected false pair fraction for our sample. As we also include late-stage mergers and not only widely separated pairs, based on this a more realistic estimate of the amount of interlopers would probably be ∼4 per cent.

Furthermore, several studies have shown that the morphology of isolated star-forming galaxies at higher redshifts is often clumpy and irregular (Bournaud, Elmegreen & Elmegreen 2007; Genzel et al. 2008, 2011; Elmegreen et al. 2009; Kriek et al. 2009; Law et al. 2009, 2012; Förster Schreiber et al. 2011a,b; Wisnioski et al. 2011a; Wuyts et al. 2012). This potentially biases our visual classification as inclusion of such systems will artificially enhance the number of selected mergers and hence the estimated fraction of mergers in our sample. As described below both parametric and visual classification schemes will be subject to this bias. Hence, what is described as a merger in the present selection might in fact be a galaxy with a clumpy and irregular light distribution appearing like a merger remnant. This caveat should be kept in mind when evaluating the merger candidates presented here and elsewhere. In the remainder of the paper we will therefore use the shorthand *merger* for *likely merger candidates*.

The visual inspection is not only used to select morphologically disturbed systems. Inspecting the full grism spectra, as well as the one-dimensional collapsed grism spectra, of the individual objects, we are able to discard objects without any emission line features. Without emission line features creating a star formation map as described in Section 4 is impossible. Assuming that the estimated SFR, mass and redshift are correct, the fact that these objects lack emission line features make them very interesting in themselves, as they might be highly dust-obscured systems blocking the star formation emission. However, these objects are ignored for the present study. If an emission line feature on the other hand is observed, i.e. the (collapsed) emission line flux is roughly larger than $\sim 10^{-16}$ erg s$^{-1}$ cm$^{-2}$ (see Section 3.2), the object is included in our sample and we attempt to create an emission line map. However, as noted in Section 3.2 and as we will see in Section 5 this

does not necessarily mean that the S/N per pixel in the full grism spectrum is good enough to create an emission line map.

Visually inspecting the grism spectra also ensures that any strong contamination is due to the different components of the merging system and not due to interlopers.

From the parent sample of 352 catalogue-selected objects, the visual inspection discards 292 objects as they appear to be isolated 'normal' galaxies (252/292), or having high contamination not stemming from the merging components (13/292), or having no obvious emission line features in their spectra (24/292 corresponding to $7^{+3}_{-2}$ per cent of the 352 catalogue-selected objects). Hence, our final sample of (potential) mergers from six GOODS-S and 24 COSMOS 3D-*HST* pointings consists of 60 systems, corresponding to $\sim 17^{+4}_{-4}$ per cent of the 352 catalogue-selected objects, or approximately 10–13 per cent if we correct for the expected fraction of false pair interlopes. Here the confidence intervals are the 95 per cent quantiles of the $\beta$ distribution following Cameron (2011). This merger candidate fraction is on the high side compared to what is generally found in the literature (see e.g. fig. 1 in Lotz et al. 2011; Williams, Quadri & Franx 2011), again suggesting that a fraction of the visually identified mergers may be single objects with a blotchy distribution of young stars which increases the apparent merger fraction. The obtained merger fraction is subjective as it relies on a visual assessment of disturbance. As described above, also potential galaxy interlopers which have passed the subjective visual inspection could be biasing our sample towards higher merger fractions. Williams et al. (2011) used a mass-selected sample ($\log(M/\mathrm{M}_\odot) > 10.5$) of galaxy pairs when estimating a major merger fraction of ∼5 per cent. This could also account for part of the discrepancy, as we are not only looking at distinct pairs of galaxies and use a flux limit as opposed to a mass limit in the selection process. With an average merger fraction just below 10 per cent at $z \sim 1$ the merger fractions summarized in fig. 1 of Lotz et al. (2011) which includes samples selected on both mass and luminosity cuts is somewhat closer to the $17^{+4}_{-4}$ per cent (∼10–13 per cent if corrected for interlopes) reported here.

The selection cuts in Table 1 positions all 60 3D-*HST* mergers in the blue cloud of star-forming galaxies (Strateva et al. 2001; Bell et al. 2004) in colour–magnitude diagrams, which implies (as expected) that the selected mergers are mainly gas-rich 'wet' mergers. We note however, that this may be very different for mass-selected samples where no limits have been imposed on the overall SFR of the objects.

In Fig. 1 we show the $m_{F140W}$ magnitude distribution of the 60 3D-*HST* merger candidates. In Figs 2 and 3 we plot them together with the selection regions from Table 1 (grey shaded regions) as large solid symbols. The small grey points represent the 292 objects discarded by the visual classification, i.e. the general galaxy populations satisfying the selection cuts in Table 1. In Fig. 3 the distributions of SFR, sSFR, $z_{\mathrm{grism}}$ and $M_*$ for the 60 merger candidates are shown as histograms on the axes of the scatter plots. In both the histograms in Figs 1 and 3, the dotted lines correspond to the 16th and 84th percentiles of the distributions, and the dashed lines show the median values. In Section 6 we will use these values to determine the parameter space to sample when simulating 3D-*HST* grism spectra.

Visual inspection is a more subjective way of selecting mergers than for instance empirically established parametric merger classification schemes like for instance the Gini ($G$), $M_{20}$ and *CAS* selections (e.g. Conselice 2003; Lotz, Primack & Madau 2004; Papovich et al. 2005; Lotz et al. 2006, 2008a,b; Scarlata et al. 2007; Conselice et al. 2008; Conselice, Yang & Bluck 2009). Both parametric and visual classification schemes have advantages and disadvantages. Determining a merger population based on parameters ensures that the selection is done in a consistent and uniform way for all objects. However, at redshifts where the NIR morphology is not fully understood and where galaxies look clumpy and irregular as described above, and where disturbed morphologies are prominent without necessarily being part of a recent merger, a parametric classification scheme might fall short of a visual classification. On the other hand visual classification is potentially biased by the subjectivity of the classifier. Nevertheless, the human eye is known to be excellent at detecting and distinguishing features in noisy images

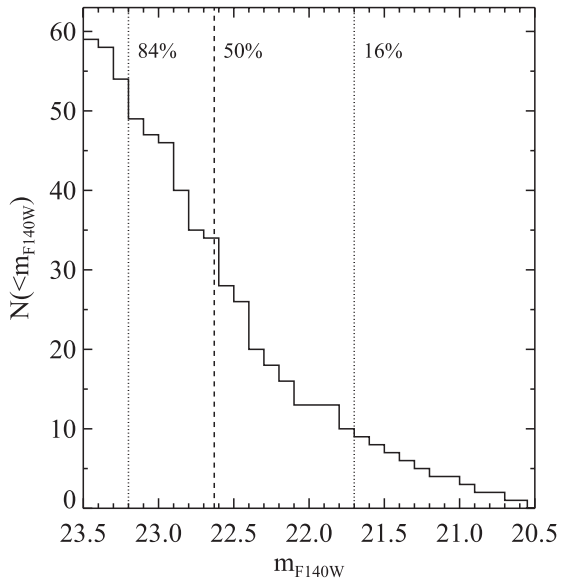


**Figure 1.** The cumulative distribution of $m_{F140W}$ magnitudes for the 60 3D-*HST* mergers. The dotted lines indicate the 16th and 84th percentiles of the distribution whereas the dashed line shows the distribution median. The 16th and 84th percentile values are used when defining the parameter space for the simulated grism spectra in Section 6.

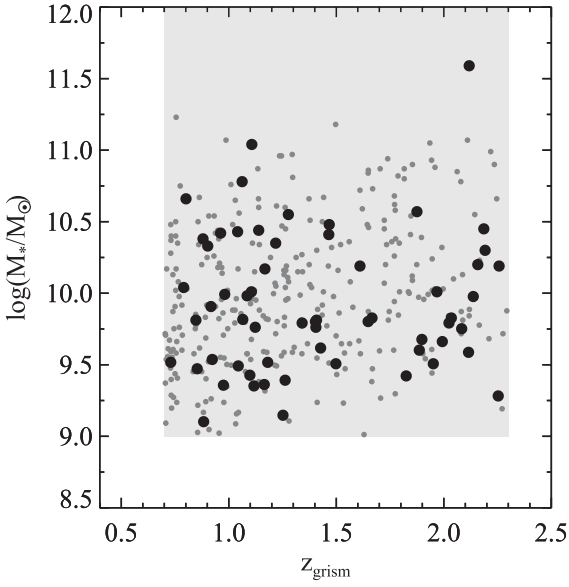


**Figure 2.** The distribution of inferred stellar mass as a function of redshift for the 60 3D-*HST* merger candidates (large points). The small grey points represent the 292 objects discarded by the visual inspection and the grey shaded region shows the selection region from Table 1.

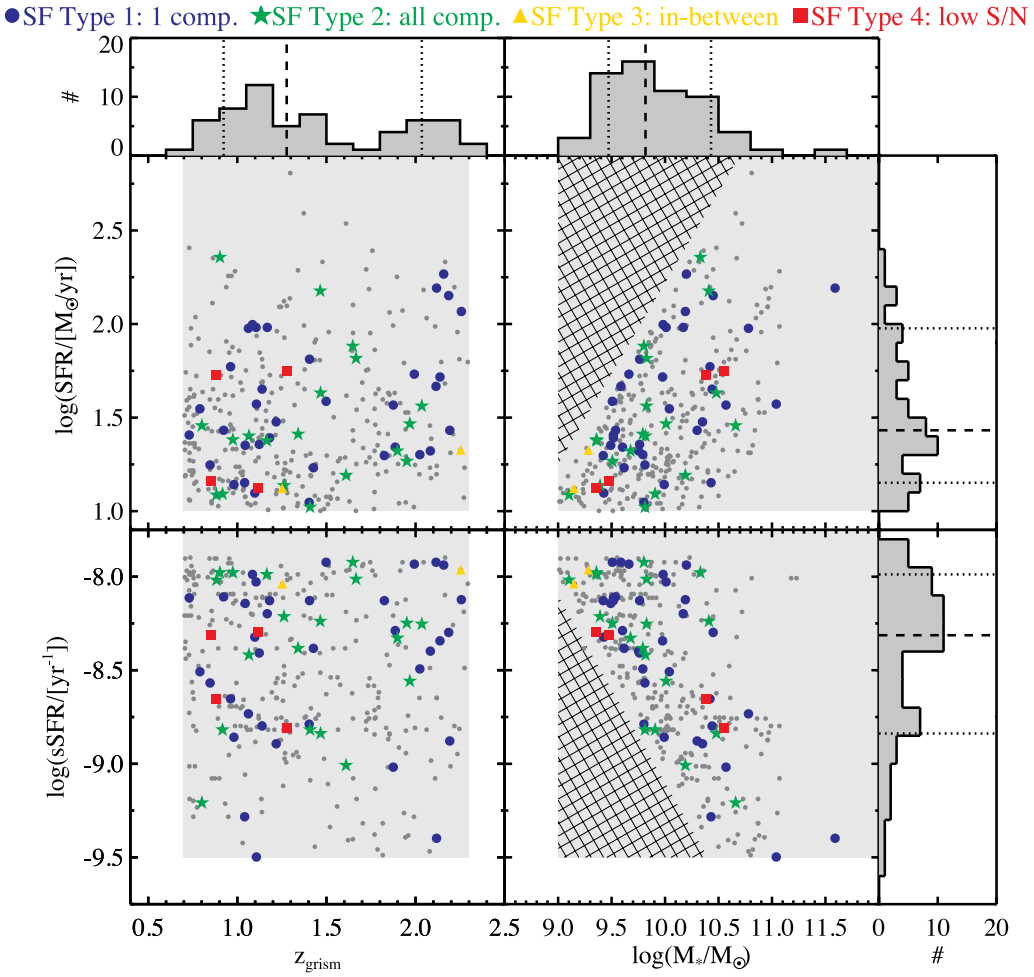


**Figure 3.** The 60 3D-*HST* mergers (large symbols) plotted in the main region of the catalogue selection space given in Table 1 (grey shaded regions). The small grey points represent the 292 objects discarded by the visual inspection. The hashed regions are empty due to our selection criteria. The histograms attached to the scatter plots show the distribution of $z_{\rm grism}$, $M_*$, SFR and sSFR for the 60 mergers. The dotted and dashed lines in the histograms indicate the 16th and 84th percentiles and the median of the distributions, respectively. These values are used to define the parameter space of the simulated grism spectra described in Section 6. The different symbols (and colours) indicate the morphology of the emission line maps (SF type) described in Section 5 as indicated above the panels. No obvious trends are found between the SF morphology and the SFR, sSFR, redshift or stellar mass.

and spectra and arguably minimizes the bias of the clumpy irregular morphology of high-$z$ systems.

To ease comparison with the extensive literature using parametric merger classifications we have estimated the $G$, $M_{20}$, $C$, $A$ and $S$ morphological parameters for the 60 visually selected merger candidates and the 292 visually discarded objects as shown in Appendix A. The selected candidates partially satisfy the empirical parametric merger selection but in general seem to be an average subset of the parent distribution, i.e. not distinguishing itself clearly from it. Assuming that the 60 merger candidates are reliable therefore speaks in favour of using visual classification when the NIR morphology is complicated, as a parametric $GM_{20}CAS$ classification would not be able to clearly distinguish the 60 merger candidates from the parent population.

Despite the limitations of a visual selection of mergers and the only partial agreement with the empirical parametric classifications (Appendix A), we believe that the advantages of the visual classification scheme described above outweighs a 'blind' parametric selection for a study like the one presented here. Furthermore, we are probing an unexplored regime (NIR at high redshift) and the current parametric methods might not be appropriately calibrated and tested here and we have therefore chosen to use the visual selection in the reminder of this paper.

## 4 EMISSION LINE MAPPING

To quantify the extent of (unobscured) star formation in the 60 3D-*HST* mergers described in the previous section, we rely on the spatial information of the H$\alpha$ and [O III] emission lines that the slitless grism spectroscopy provides. From the grism spectra we create emission line maps by subtracting a model of the continuum light in the grism spectra such that only the probed emission line feature is remaining. This can then be mapped back on to the NIR continuum light distribution of the object. In practice we

(i) create a 2D continuum model for the grism spectrum;
(ii) subtract this continuum model from the 2D grism spectrum itself;

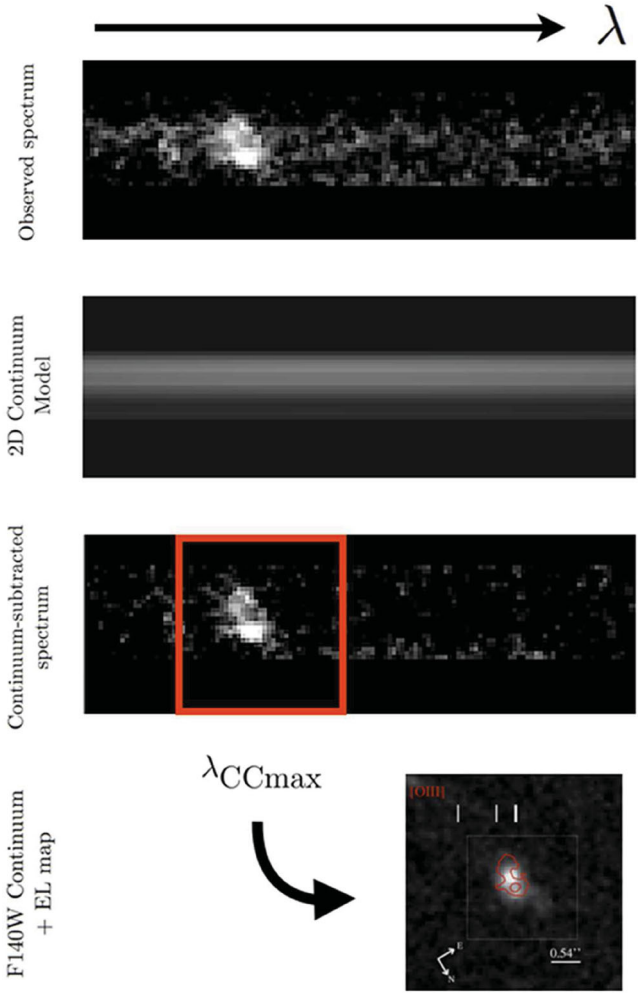


**Figure 4.** Steps performed to obtain the emission line (star formation) maps as described in Section 4. The top panel shows a standard 3D-*HST* spectrum with a prominent emission line feature. The 2D continuum model, a set of polynomial fits to the observed spectrum when excluding the emission line feature (Section 4.1), is shown just below that. The third panel shows the spectrum from the top panel after subtraction of the 2D continuum model. The red square marks the emission line map cut-out at $\lambda_{\rm CCmax}$ obtained by cross-correlating the NIR *F140W* thumbnail of the object (grey-scale bottom panel) with the continuum-subtracted spectrum. The bottom panel illustrates how this emission line map cut-out is mapped back (red contours) on to the continuum image.

(iii) cross-correlate the *F140W* thumbnail with the continuum-subtracted spectrum to map the (cut-out) continuum-subtracted thumbnail back on to the *F140W* thumbnail.

Each of these steps is described in detail in the following subsections and is illustrated in Fig. 4.

### 4.1 Continuum modelling and subtraction

The 2D continuum models we subtract from the 3D-*HST* spectra are based on a third-order polynomial fit to a one-dimensional spectrum. The 1D spectra are obtained from a weighted sum of the individual lines in the 2D spectra. The polynomial fit to the 1D spectrum is turned back into a 2D continuum model by concatenating rows with the 1D polynomial form weighted by a 'slit-profile' obtained from the columns blueward and redward of the probed emission line feature in the full 2D spectrum. Subtracting this model from the 3D-*HST* spectrum returns a two-dimensional emission line map as illustrated in Fig. 4, where all that is left is the emission line feature. This approach is similar to the one used in Nelson et al. (2012). Often when dealing with slitless spectroscopy, and the 3D-*HST* grism spectra in particular, the goal is to remove contamination in a systematic manner. However, we relied on visual inspection to remove badly contaminated objects, since mergers per definition are contaminated. Remaining contamination not affecting the continuum flux of the merger was masked out when modelling the continuum before subtraction.

### 4.2 Constructing emission line maps

We used a simple cross-correlation between the NIR *F140W* thumbnail continuum image of each object and the corresponding full 2D emission line map in order to map the emission line map back on to the NIR image. In practice we calculate

$$\mathrm{CC}(\lambda) = \sum_{i}^{N_{\rm width}} \sum_{j}^{N_{\rm width}} f_{i,j,F140W}\, f_{i,j,\mathrm{ELmap}} \qquad (1)$$

for each of the first $k = N_{\rm 2D} - N_{\rm width}$ columns in the full 2D emission line map, where $N_{\rm 2D}$ is the number of columns in the 2D emission line map and $N_{\rm width}$ is the width of the *F140W* thumbnail. The $f_{i,j,F140W}$ and $f_{i,j,\mathrm{ELmap}}$ is the flux in the pixel $(i, j)$ for the *F140W* thumbnail and 2D emission line map cut-out (indicated by the red box in Fig. 4), respectively.

The maximum of the cross-correlation function, CC, indicates the wavelength, $\lambda_{\rm CCmax}$, where there is the largest overlap between the NIR light distribution of the object and the $k$th cut-out of the full emission line map. The $\lambda_{\rm CCmax}$ corresponds to the $k$th column of the 2D emission line map plus $N_{\rm width}/2$.

In Fig. 5 we show a collection of emission line maps (red contours) from our 3D-*HST* merger sample. The individual maps correspond to the region at $\lambda_{\rm CCmax}$ that has been mapped back on to the NIR continuum image as illustrated in Fig. 4. In each map we have marked the relative location of [N II] λλ6548, 6583, Hα λ6563, [S II] λλ6716, 6730 and Hβ λ4861, [O III] λλ4959, 5007 for the Hα and [O III] maps, respectively. In some cases the [O III] doublet is marginally resolved as seen in the upper left emission line map in Fig. 5. The Hα–[N II] composite is however not resolved in the 3D-*HST* grism resolution. We do not attempt to de-convolve these emission lines when creating the emission line maps. Assuming that $F_{[\rm O\,III]\,\lambda5007} = 3F_{[\rm O\,III]\lambda4959}$ the redshift uncertainty imposed by ignoring the [O III] doublet is only 0.0024. This is less than the quoted average 3D-*HST* redshift precision of $0.0034(1+z)$ (Brammer et al. 2012) and is therefore not affecting the conclusions of this study.

The different 'morphologies' of the emission line maps in Fig. 5 will be addressed in Section 5. In Appendix B we show the full sample of 3D-*HST* merger emission line maps.

## 5 RESULTS: THE SPATIAL EXTENT OF STAR FORMATION IN HIGH-$z$ MERGERS

As noted in the Introduction, star formation and mergers are important parts of understanding how high-$z$ galaxies evolved into the galaxies we observe in the low-$z$ Universe. In the previous sections we have described how we select the mergers from the 3D-*HST* data, and subtract the continuum light in the spectra to create the emission line (star formation) maps. In this section we characterize the morphological type of the spatial extent of the star formation in the

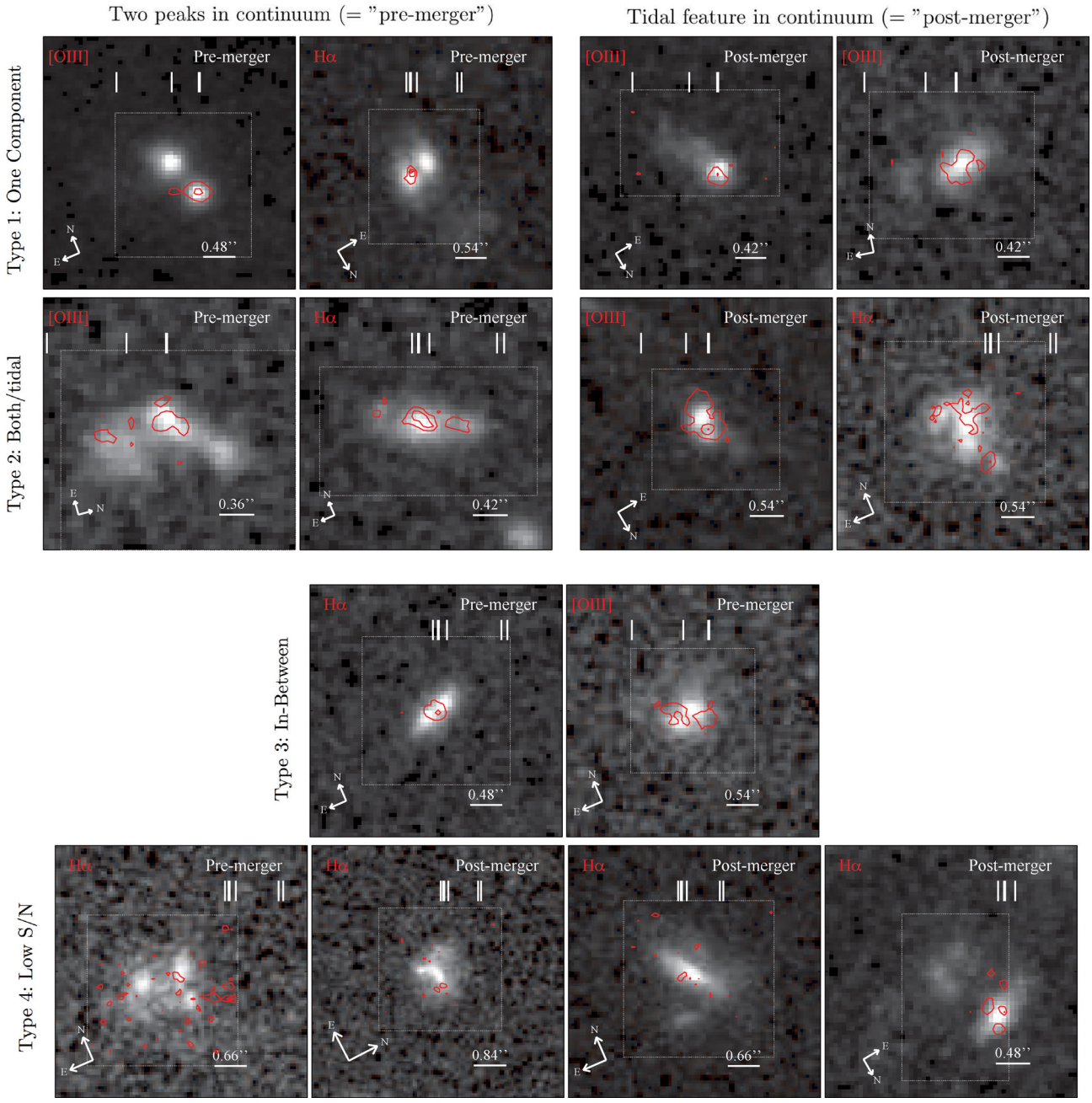


**Figure 5.** Examples of H$\alpha$ and [O III] emission line maps (red contours) plotted on the WFC3 *F140W* thumbnails (grey-scale) for a sub-subsample of the 60 3D-*HST* mergers. The dashed boxes indicate the mapped region. Each row represents one morphological type of star formation distribution as described in Section 6.2. From top to bottom each row show maps of SF type 1 ('one component' maps), SF type 2 ['both (all) component' maps], SF type 3 ('in-between' maps) and SF type 4 ('low S/N' maps). The Type 1 and 2 maps (first two rows) have been divided into pre- (left) and post-mergers (right). The vertical white lines indicate the relative distance between [N II] $\lambda\lambda$6548, 6583, H$\alpha$ $\lambda$6563, [S II] $\lambda\lambda$6716, 6730 and H$\beta$ $\lambda$4861, [O III] $\lambda\lambda$4959, 5007 for the H$\alpha$ and [O III] maps, respectively. The full sample of emission line maps is shown in Appendix B.

60 3D-*HST* mergers. However, we first divide our sample into two different kinds of mergers: the 'pre-mergers' and the 'post-mergers'. By pre-mergers we mean objects that show multiple clearly distinct and pronounced continuum peaks in the NIR images, i.e. the optical continuum emission comes from multiple objects in the process of merging or about to merge. Examples of those are shown to the left in the two top panels of Fig. 5. The post-mergers, on the other hand, are systems that have (presumably) undergone merging and now appear to be dominated by a nuclear feature in the continuum with pronounced tidal features surrounding it. Examples of these systems are shown to the right in the two top panels in Fig. 5. Dividing the 60 mergers into these two subsamples return 32 pre-mergers and 28 post-mergers. We note that the distinction between pre- and post-mergers is (operatively) our distinction to guide-the-eye when classifying and inspecting the emission line maps of the individual objects as described below. The identification with the merger phases is plausible, but will need more modelling.

To characterize the location and the spatial extent of the star formation in the 3D-*HST* mergers we categorize the star formation maps into the following four morphological types (SF type).

(1) *One component.* The star formation in the primary emission line feature is significantly stronger than any secondary emission line feature. The threshold used is $F_p > 2.5\ F_s$, where $F_p$ and $F_s$ are the estimated aperture flux of the primary and secondary emission line feature, respectively. For the pre-merging systems the primary emission line feature corresponds to one of the multiple objects and for the post-mergers it refers to either the nuclear region or a tidal feature.

(2) *Both (all) components.* The star formation is pronounced/detected in all (or the majority if more than two) components of the system, i.e. $F_p < 2.5\ F_s$.

(3) *In-between.* The mapped star formation appears to be emerging from in-between the merging components. None of the post-mergers shows this feature, so indeed this means in-between clearly distinguishable objects.

(4) *Low S/N.* The S/N per pixel of the emission line features in the 2D grism spectrum is too low to produce a convincing emission line map. This may be the case for extended star formation as pointed out in Section 3.2. It can also be due to very dust-enshrouded star formation making the emission lines very weak.

Each of the four rows of star formation maps in Fig. 5 shows examples of these four SF types. The results from characterizing the two classes of mergers with these four SF types are shown in Fig. 6. The error bars are obtained by bootstrapping the results, i.e. by randomly drawing 60 SF types from the results 1000 times and then using the $2\sigma$ width of the resulting SF type distributions as error bars (hence no error bar on the post-merger SF type 3 in Fig. 6, as none was found). For both the pre- and post-mergers, the star formation is most prominent in just one of the components (SF type 1) for roughly 3/5 of the objects. In roughly 1/3 of the objects, star formation was detected in all components (SF type 2). Hence, the distribution of the spatial extent of star formation among the pre- and post-mergers is consistent. In Table 2 we have listed the fractions for all 60 3D-*HST* mergers resulting from the classification of the emission line maps.

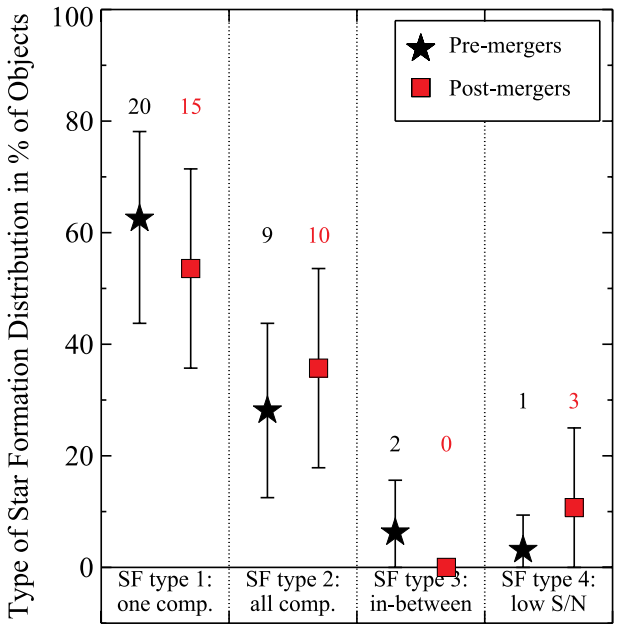


**Figure 6.** The morphological types of the star formation distribution (Section 5) observed in the 60 3D-*HST* merger candidates split into 'pre-mergers' of multiple individual objects (32 objects, black stars) and 'post-mergers' of systems with a nucleus and tidal features (28 objects, red squares). The number of objects with a given SF type is indicated above each point. The error bars are obtained via bootstrapping as described in the text. The two samples have similar star formation distributions. About 20 per cent of the objects show star formation in all merger components (individual objects or nucleus and tidal feature), whereas ∼60 per cent of the systems only show star formation in one component.

**Table 2.** The spatial extent of star formation.

| SF type | 3D-*HST* | | Simulations | |
|---|---|---|---|---|
| 1) One Comp. | $58^{+12}_{-13}$ per cent | (35/60) | $28^{+5}_{-5}$ per cent | (83/296) |
| 2) Both (all) comp. | $32^{+12}_{-12}$ per cent | (19/60) | $59^{+6}_{-6}$ per cent | (175/296) |
| 3) In-between comp. | $3^{+5}_{-3}$ per cent | (2/60) | $0^{+0}_{-0}$ per cent | (0/296) |
| 4) Low S/N per pixel | $7^{+8}_{-5}$ per cent | (4/60) | $13^{+4}_{-4}$ per cent | (38/296) |

*Note.* Uncertainties are obtained via bootstrapping as described in the text. See Fig. 7 for a plot of these values.

The difference in the rates of objects with prominent star formation in just one component (SF type 1) and mergers with star formation of type 2 might be a consequence of dust obscuration. We are only able to probe the unobscured star formation, so in cases where one component (or the tidal feature) is much more dust-obscured than the other we would end up with star formation maps of type 1. The discrepancy between the rates could also be due to different SFRs in the different components. Since the mergers are selected based on morphology and we do not have any kinematic information, the fraction of SF type 1 objects might be biased by chance superpositions of objects on the sky at different redshifts, such that we only see line emission from one object in the NIR. As described in Section 3.3 we expect approximately 4–7 per cent of such objects due to the modest distances of ∼8.5 kpc involved.

The results indicate that most mergers happen between objects of different gas fractions and/or different SFR, i.e. two merging components with significantly different properties. We will show below that this is backed up by an initial comparison with simulated mergers.

In Fig. 3 the different SF types are represented by different symbols to look for dependencies between the morphology of the star formation maps and SFR, sSFR, $z_{grism}$ and $M_*$. These quantities are obtained on the *total* photometry of the merging components as only a single photometric ID was assigned to each merger and hence includes the flux of the total system. The absence of correlations seen in Fig. 3 suggests that all star formation morphologies occur at all redshifts irrespective of SFR and mass.

## 6 SIMULATING 3D-*HST* SPECTRA

With the exceptional data of the 3D-*HST* merger sample presented above, we can perform comparisons with the star formation produced in simulated mergers at high redshift. Current high-resolution merger simulations are able to predict the spatial distribution of star formation in mergers and produce simulated images by including the emission by young, newly formed stars and the transfer of starlight through gas and dust (Cox et al. 2006, 2008; Jonsson, Groves & Cox 2010). Lotz et al. (2008a,b, 2010a,b) used these and similar simulations to describe the correlations between the rest-frame optical morphology of mergers, their mass ratios, total star formation, projected size, gas fractions and merger time-scales, enabling comparisons with observations.

Simulations have shown examples of star formation triggered by direct galaxy interaction, star formation originating in the central cores of the individual merging components and star formation appearing in tidal features. In the nearby Universe, many examples of such features have been found e.g. in the Antennae galaxies (Wang et al. 2004). Whether the predictions of simulations are also representative of the star formation in mergers at $z \sim 1.5$, i.e. when the Universe was only 3–4 Gyr old, have not been tested yet. With 3D-*HST*, the sample size of data with both rest-frame optical morphology *and* star formation morphology is becoming large enough that we can start looking at a *population* (snapshot) of mergers instead of individual case studies, and hence comparisons with predictions from simulations become feasible. In this section we make an initial illustrative attempt at comparing state-of-the-art merger simulations with the observational results from 3D-*HST*. In the following we describe how we create simulated WFC3 G141 grism spectra from a small initial set of high-resolution simulated mergers.

### 6.1 SPH merger simulations

Knowledge about both the spatial and spectral extent of the objects is crucial for simulating grism spectra. As input for our grism simulations we use three-dimensional data cubes of simulated mergers. These input data cubes are based on the simulations described in Younger et al. (2008) and are designed in the spirit of the Cox et al. (2006, 2008) simulations. The simulations are *N*-body/SPH simulations from the GADGET code (Springel, Yoshida & White 2001) from which simulated observations are generated with the radiative transfer code SUNRISE (Jonsson 2006; Jonsson et al. 2010). For our initial comparison of simulations with actual data, we use the three models listed in Table 3. The three simulations are all of mass ratio 2:1 and the two merging objects in each simulation both have a gas fraction ($f_{\rm gas}$) of 40 per cent, making them 'wet' mergers like the 3D-*HST* systems and mimicking the suggested gas fraction of $z > 1$ galaxies (Daddi et al. 2010; Tacconi et al. 2010). The three mergers happen at three different relative orbital inclinations ($\Theta$) of the two merging components. Hence, what we test here is the effect of orientation on the detected star formation distribution. We further have a series of time-steps or snapshots of each galaxy ($N_{\rm t}$) and a set of viewing angles ($N_{\rm view}$) that we can simulate spectra for. Thus, the simulation parameter space sampled here is spanned by time, orientation of the two mergers, and viewing angle. As described below, we combine this with a set of parameters determined by the 3D-*HST* sample to define the total parameter space to be covered by the simulated spectra.

### 6.2 Simulating 3D-*HST* grism spectra

Simulating the grism spectra from the merger simulation output data cubes presented above is fairly straightforward. The mock grism spectra are created by dividing the data cube into wavelength slices, i.e. images corresponding to a 'filter' of width $\Delta\lambda$. Offsetting or dispersing this sequence of images and co-adding the fluxes results in a grism spectrum. Using this approach, we turn the input data cubes into a sequence of simulated WFC3 G141 grism spectra. We use a pixel scale of 0.06 arcsec and a spectral resolution of $\Delta\lambda = 22$ Å according to the 3D-*HST* grism spectra characteristics described in Brammer et al. (2012). For the *HST* point spread function (PSF) we use a TINY TIM PSF[2] and for the system throughput we used the G141 sensitivity curve.

We use the parameter space of the observed merger sample from 3D-*HST* to define the parameter space of the simulations. By rescaling each data cube we simulate grism spectra corresponding to the 16th and 84th percentiles of the magnitude ($m_{F140W}$), redshift ($z_{\rm grism}$) and SFR distributions of the 3D-*HST* data as indicated by the dashed lines in the corresponding histograms in Figs 1 and 3.

To adjust the SFR of the data cubes before turning them into grism spectra, we assume that the SFR to H$\alpha$-flux conversion follows the empirical relation of Kennicutt et al. (1994):

$$\frac{\rm SFR}{[\rm M_\odot\ yr^{-1}]} = \frac{1}{1.26 \times 10^{41}}\ \frac{L_{\rm H\alpha}}{[\rm erg\ s^{-1}]}. \quad (2)$$

This relation assumes a Salpeter (1955) IMF and is applied to the emerging SFR, i.e. after the effects of extinction are taken into account by SUNRISE. The $m_{F140W}$ is obtained by scaling the flux (including emission lines) integrated over the *F140W* passband independently. Combining the values from Table 3 with these data-determined parameters, we end up with a sample of 336 simulated spectra spanning the parameter space ($N_{\rm t}$, $N_{\rm view}$, $\Theta$, $m_{F140W}$, $z$, SFR).

Added to the raw mock grism spectra are Poisson noise and noise terms corresponding to the read noise and dark current quoted on the WFC3 website, as well as the background sky levels presented in Brammer et al. (2012).

In Fig. 6 we present a sequence of simulated G141 grism spectra. The spectra shown have various combinations of $N_{\rm t}$, $N_{\rm view}$, $\Theta$, $m_{F140W}$, $z$ and SFR. The thumbnails on the left are the noise-free simulated *F140W* images of the objects.

### 6.3 Creating star formation maps of simulated spectra

To create the star formation maps for the simulated spectra, we treat them in exactly the same way as the actual 3D-*HST* spectra (see Section 4). First, we visually inspect the spectra to make sure that an emission line feature is available; for some of the faint magnitude, low-SFR combinations the emission lines do not show up in the noise-added spectra. Having eliminated spectra without emission line features, as well as cases of viewing angle and time-step were the two merging objects could not be distinguished, the sample of 336 simulated spectra is reduced to 296. For these 296 spectra, we create emission line maps by the method described in Section 4.

As for the actual 3D-*HST* data, we characterize the 296 emission line maps of the simulated spectra according to the four SF types described in Section 5. The results from this classification are shown in Table 2 together with the results for the 3D-*HST* mergers. The simulated spectra in Fig. 6 show examples of both spectra resulting in star formation maps of type 1 (first three spectra) and type 2 (last three spectra).

**Table 3.** The simulated 3D input data cubes.

| Name | $N_{\rm t}$ | $N_{\rm view}$ | Mass ratio[a] | $f_{\rm gas}$ | $\Theta$ |
|---|---|---|---|---|---|
| Sim. 1 | 6 | 3 | (Sb) 2:1 (Sc) | 0.4:0.4 | 30° |
| Sim. 2 | 5 | 3 | (Sb) 2:1 (Sc) | 0.4:0.4 | 90° |
| Sim. 3 | 3 | 3 | (Sb) 2:1 (Sc) | 0.4:0.4 | 150° |

[a]Parenthesis gives disc model (Younger et al. 2008).

[2] http://www.stsci.edu/hst/observatory/focus/TinyTim

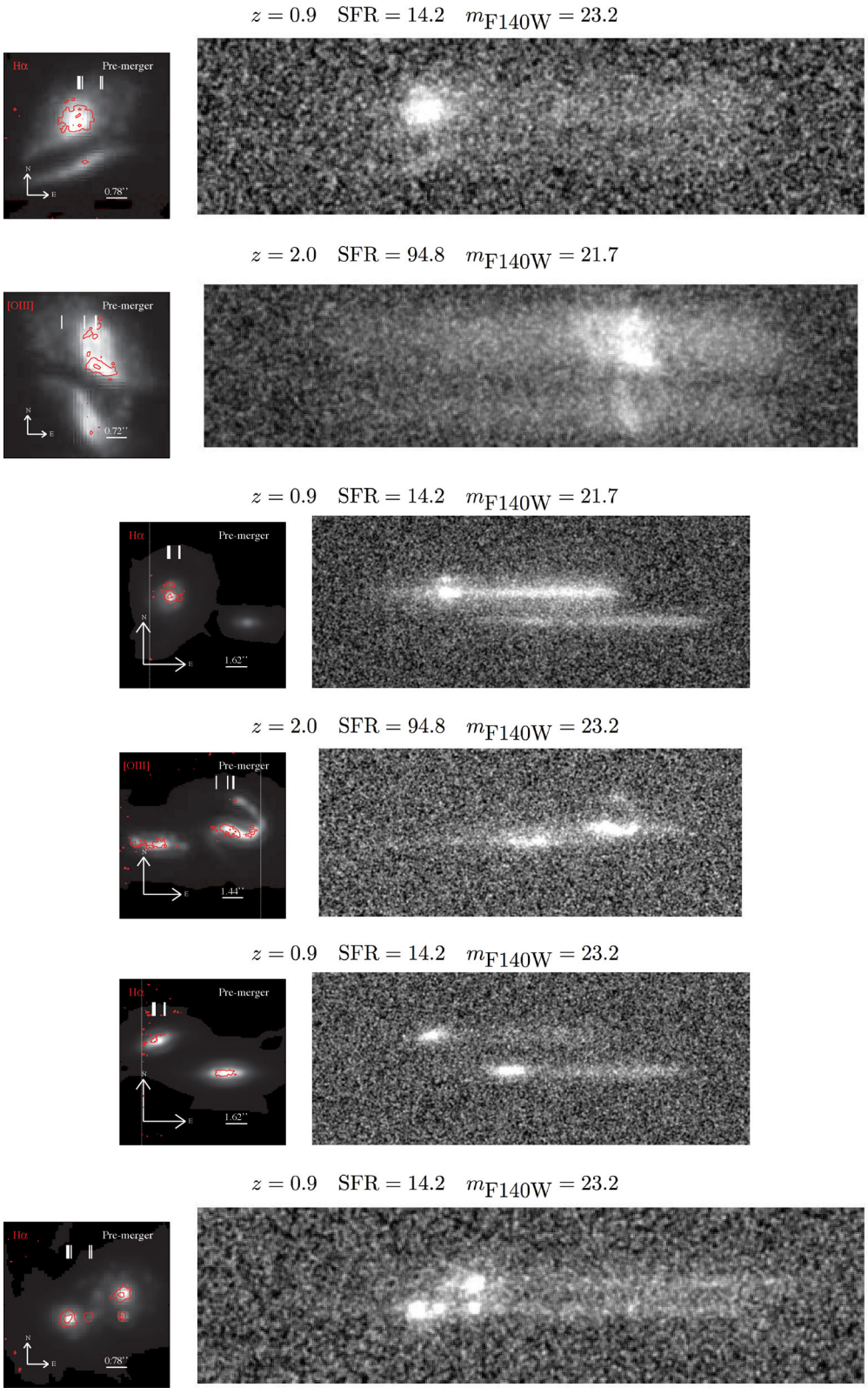


**Figure 7.** Examples of simulated 3D-*HST* data based on simulated observations of *N*-body/SPH mergers generated with the radiative transfer code SUNRISE. The thumbnails (left) are emission line maps similar to the ones shown for the 3D-*HST* data in Fig. 5. The first three spectra (right) result in star formation maps of SF type 1, while the last three result in SF type 2 star formation maps. Various combinations of SFR, $m_{F140W}$, $z$, time-step in the merging of the components ($N_t$), viewing angles ($N_{\rm view}$), and initial relative orbital inclination of the two merging components ($\Theta$) are shown.

### 6.4 Comparing the 3D-*HST* data with simulations

We compare the 3D-*HST* SF types we inferred in Section 5 with the simulated SF types in order to investigate how e.g. SFR and viewing angle influence the frequencies of different types of mergers from the characterization of the extent of star formation in mergers. In Fig. 8 the SF types of the full sample of 60 3D-*HST* mergers (blue circles) are shown together with the SF types of the 296 simulated spectra of the three mergers from Table 3 (green triangles). The plotted percentages are given in Table 2. The error bars are again obtained via bootstrapping. The comparison needs to be done with care, as the sample of simulated mergers from Table 3 does not span the gas fraction and mass ratio dimensions of the parameter space, expected to influence the 'observability' of star formation (Lotz et al. 2010a,b, 2011), as they are fixed at 40 per cent and 2:1, respectively (see Section 6.1). Nevertheless, our analysis shows how the 3D-*HST* survey enables a direct comparison of predictions from simulations with an extensive sample of high-$z$ mergers.

Despite the limitations of the spanned simulation space, it seems that the fraction of spectra where the S/N per pixel is too low to create an actual emission line map is fairly consistent. Likewise, the fraction of cases where the star formation seems to emerge from in-between the merging components (SF type 3) is comparable: in fact we do not find any objects in this category among the simulated spectra. Looking at the two SF type 3 cases we find for the data (third row of Fig. 5) could indicate that the reason we are not seeing star formation from the components themselves is due to dust obscuration rather than more pronounced star formation in-between the components. To find similar trends in the simulated emission line maps we would need to investigate a range of gas fractions rather than just the $f_{\rm gas} = 40$ per cent cases presented here. This is however beyond the scope of this initial comparison.

From Fig. 7 it is also evident that the simulated spectra, on average, have twice as many star formation maps where both components have pronounced star formation (SF type 2), i.e. nearly 2/3 of the simulated maps, as compared to ∼1/3 for the 3D-*HST* star formation maps. Correspondingly, the fraction of single-component emission line maps is significantly lower for the simulations than for the observations. As the simulations assume fairly similar properties between the two merging components (same gas fraction, similar mass in the form of major mergers as opposed to minor mergers, same dust content and total SFR), this suggests that the majority of mergers do not happen between such galaxies. According to the 3D-*HST* data, only ∼1/3 of real mergers seem to happen between galaxies of similar properties. For example, different gas fractions or a larger gap between the masses (minor mergers) could change this picture, in agreement with the results presented in Section 5.

Also, the distribution of orbits and orientations of the merger components could play a significant role here. The presented simulations consist of both prograde–prograde (Sim. 1), prograde–polar (Sim. 2) and prograde–retrograde (Sim. 3) mergers. We find a deficit of SF type 1 mergers among the Sim. 1 emission line maps, in good agreement with the notion that prograde–prograde mergers generally result in more symmetric star formation (di Matteo et al. 2007). Hence, several factors might play a role in the difference found between the 3D-*HST* and simulated emission line (star formation) maps.

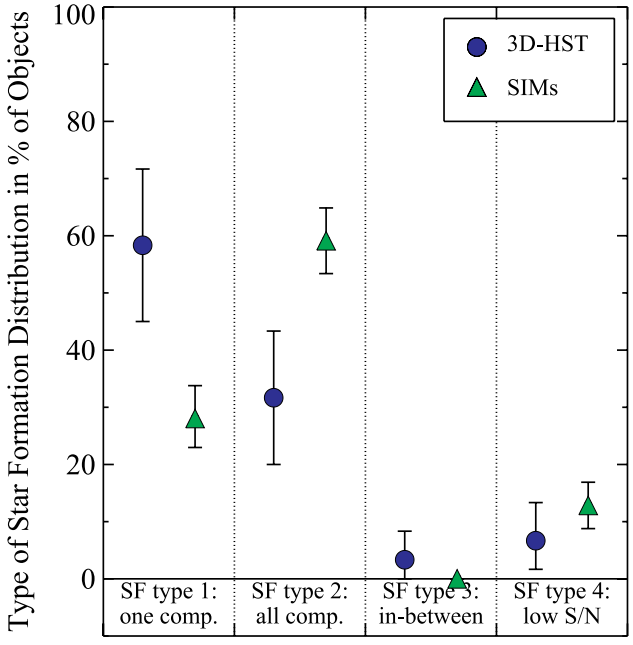


**Figure 8.** Comparing the spatial extent of star formation (SF type; Section 5) in the 60 3D-*HST* mergers (blue circles) with the 296 simulated spectra (green triangles). Each point has been assigned an error-bar obtained via bootstrapping. Direct comparisons should be done with care due to the limited size of the parameter space the simulations span. Nevertheless, it is evident that the simulations show many more cases where star formation is seen in both the merging components than the 3D-*HST* data do, indicating that the majority of mergers have different gas fractions and/or mass ratios prior to merging.

## 7 CONCLUSION

We have presented a sample of galaxy merger candidates with three-dimensional (RA, Dec. and λ) spectroscopy at redshift $z \sim 1.5$. The sample consists of 60 morphologically selected mergers from the Hubble treasury slitless grism survey 3D-*HST* with total masses and SFRs for the systems derived from multiwavelength photometry. From the slitless grism spectroscopy we created emission line maps of the rest-frame optical emission lines H$\alpha$ and/or [O III] as a proxy for the *spatial* extent of the unobscured star formation. Our results go towards a comprehensive empirical picture of where star formation happens in galaxy mergers at $z \sim 1.5$ when the cosmic star formation and merger rate were at their peak.

We have also carried out an illustrative comparison of the 3D-*HST* mergers to recent SPH simulations of galaxy mergers which include star formation and dust extinction. This small sample of simulations points the way towards more extensive simulation programs aimed at spanning the full parameter space of the observations.

The main conclusions of the present study are the following.

(i) The spatial distribution of star formation in $z \sim 1.5$ candidate mergers shows a broad range of morphologies. It is often concentrated in a single, compact region, but can also be located in tidal tails or in-between the main stellar bodies of the progenitors.

(ii) In the majority ($58^{+12}_{-13}$ per cent) of the early-stage, pre-coalescence mergers, the star formation is significantly more pronounced in just one of the merging components. This is likely due to different gas fractions of the progenitors. Alternatively, dust content may differ in quantity or configuration.

(iii) The star formation morphologies show no clear correlations with the estimated SFR, sSFR, $z_{\rm grism}$ and $M_*$, suggesting that all star formation morphologies are present at all epochs irrespective of SFR and mass.

(iv) Simulated mergers among galaxies with similar masses and similar gas fractions typically predict similarly intense star formation in both merger components, at odds with the observations: as opposed to $32^{+12}_{-12}$ per cent of the observed mergers, as many as $59^{+6}_{-6}$ per cent of the simulated mergers show detectable star formation in both components. Together with the large fraction of early-stage, pre-coalescence mergers with star formation in just one component, this discrepancy supports the notion that $z \sim 1.5$ mergers typically occur between galaxies with distinctly different properties such as gas fraction, mass and/or SFR.

## ACKNOWLEDGEMENTS

We acknowledge funding from ERC grant HIGHZ no. 227749. This work was funded in part by the Marie Curie Initial Training Network ELIXIR of the European Commission under contract PITN-GA-2008-214227. The work was mainly done while KBS was a member of the International Max Planck Research School for Astronomy and Cosmic Physics at the University of Heidelberg (IMPRS-HD), Germany. This work is based on observations taken by the 3D-*HST* Treasury Program with the NASA/ESA *HST*, which is operated by the Association of Universities for Research in Astronomy, Inc., under NASA contract NAS5-26555.

## REFERENCES

Barnes J. E., Hernquist L., 1996, ApJ, 471, 115
Barton E. J., Geller M. J., Kenyon S. J., 2000, ApJ, 530, 660
Barton E. J., Arnold J. A., Zentner A. R., Bullock J. S., Wechsler R. H., 2007, ApJ, 671, 1538
Bell E. F. et al., 2004, ApJ, 608, 752
Bell E. F. et al., 2012, ApJ, 753, 167
Bigiel F., Leroy A., Walter F., Brinks E., de Blok W. J. G., Madore B., Thornley M. D., 2008, AJ, 136, 2846
Bigiel F., Leroy A., Walter F., 2011, in Elmegreen B. G., Girart J. M., Trimble V., eds, Proc. IAU Symp. 270, Computational Star Formation. Cambridge Univ. Press, Cambridge, p. 327
Bluck A. F. L., Conselice C. J., Buitrago F., Grützbauch R., Hoyos C., Mortlock A., Bauer A. E., 2012, ApJ, 747, 34
Bournaud F., Elmegreen B. G., Elmegreen D. M., 2007, ApJ, 670, 237
Brammer G. B., van Dokkum P. G., Coppi P., 2008, ApJ, 686, 1503
Brammer G. B. et al., 2012, ApJS, 200, 13
Calzetti D., Liu G., Koda J., 2012, ApJ, 752, 98
Cameron E., 2011, Publ. Astron. Soc. Aust., 28, 128
Chabrier G., 2003, PASP, 115, 763
Conselice C. J., 2003, ApJS, 147, 1
Conselice C. J., Rajgor S., Myers R., 2008, MNRAS, 386, 909
Conselice C. J., Yang C., Bluck A. F. L., 2009, MNRAS, 394, 1956
Conselice C. J., Bluck A. F. L., Ravindranath S., Mortlock A., Koekemoer A. M., Buitrago F., Grützbauch R., Penny S. J., 2011, MNRAS, 417, 2770
Contini T. et al., 2012, A&A, 539, 91
Cox T. J., 2004, PhD thesis, University of California
Cox T. J., Jonsson P., Primack J. R., Somerville R. S., 2006, MNRAS, 373, 1013
Cox T. J., Jonsson P., Somerville R. S., Primack J. R., Dekel A., 2008, MNRAS, 384, 386
Cresci G. et al., 2009, ApJ, 697, 115
da Cunha E., Charlot S., Elbaz D., 2008, MNRAS, 388, 1595
Daddi E. et al., 2010, ApJ, 713, 686
di Matteo P., Combes F., Melchior A.-L., Semelin B., 2007, A&A, 468, 61
Elmegreen B. G., Elmegreen D. M., Fernandez M. X., Lemonias J. J., 2009, ApJ, 692, 12
Epinat B. et al., 2009, A&A, 504, 789
Epinat B. et al., 2012, A&A, 539, 92
Förster Schreiber N. M. et al., 2009, ApJ, 706, 1364
Förster Schreiber N. M., Shapley A. E., Erb D. K., Genzel R., Steidel C. C., Bouché N., Cresci G., Davies R., 2011a, ApJ, 731, 65
Förster Schreiber N. M. et al., 2011b, ApJ, 739, 45
Gallagher J. S., Hunter D. A., Tutukov A. V., 1984, ApJ, 284, 544
Genzel R. et al., 2006, Nat, 442, 786
Genzel R. et al., 2008, ApJ, 687, 59
Genzel R. et al., 2011, ApJ, 733, 101
Gnerucci A. et al., 2011, A&A, 528, 88
Hammer F., Flores H., Elbaz D., Zheng X. Z., Liang Y. C., Cesarsky C., 2005, A&A, 430, 115
Hippelein H. et al., 2003, A&A, 402, 65
Hopkins A. M., Beacom J. F., 2006, ApJ, 651, 142
Hopkins P. F., Younger J. D., Hayward C. C., Narayanan D., Hernquist L., 2010, MNRAS, 402, 1693
James P. A. et al., 2004, A&A, 414, 23
Jogee S. et al., 2009, ApJ, 697, 1971
Jonsson P., 2006, MNRAS, 372, 2
Jonsson P., Groves B. A., Cox T. J., 2010, MNRAS, 403, 17
Joseph R. D., Wright G. S., 1985, MNRAS, 214, 87
Karim A. et al., 2011, ApJ, 730, 61
Kennicutt R. C., 1983, ApJ, 272, 54
Kennicutt R. C., 1992, ApJ, 388, 310
Kennicutt R. C., 1998a, ApJ, 498, 541
Kennicutt R. C., 1998b, ARA&A, 36, 189
Kennicutt R. C., Tamblyn P., Congdon C. E., 1994, ApJ, 435, 22
Klaas U., Elsaesser H., 1991, A&AS, 90, 33
Kriek M., van Dokkum P. G., Franx M., Illingworth G. D., Magee D. K., 2009, ApJ, 705, L71
Lambas D. G., Tissera P. B., Alonso M. S., Coldwell G., 2003, MNRAS, 346, 1189
Law D. R., Steidel C. C., Erb D. K., Larkin J. E., Pettini M., Shapley A. E., Wright S. A., 2007, ApJ, 669, 929
Law D. R., Steidel C. C., Erb D. K., Larkin J. E., Pettini M., Shapley A. E., Wright S. A., 2009, ApJ, 697, 2057
Law D. R., Steidel C. C., Shapley A. E., Nagy S. R., Reddy N. A., Erb D. K., 2012, ApJ, 745, 85
Lotz J. M., Primack J., Madau P., 2004, AJ, 128, 163
Lotz J. M., Madau P., Giavalisco M., Primack J., Ferguson H. C., 2006, ApJ, 636, 592
Lotz J. M. et al., 2008a, ApJ, 672, 177
Lotz J. M., Jonsson P., Cox T. J., Primack J. R., 2008b, MNRAS, 391, 1137
Lotz J. M., Jonsson P., Cox T. J., Primack J. R., 2010a, MNRAS, 404, 575
Lotz J. M., Jonsson P., Cox T. J., Primack J. R., 2010b, MNRAS, 404, 590
Lotz J. M., Jonsson P., Cox T. J., Croton D., Primack J. R., Somerville R. S., Stewart K., 2011, ApJ, 742, 103
Mancini C. et al., 2011, ApJ, 743, 86
Melnick J., Mirabel I. F., 1990, A&A, 231, L19
Mihos J. C., Hernquist L., 1996, ApJ, 464, 641
Nelson E. J. et al., 2012, ApJ, 747, L28
Newman S. F. et al., 2012, ApJ, 752, 111
Papovich C., Dickinson M., Giavalisco M., Conselice C. J., Ferguson H. C., 2005, ApJ, 631, 101
Queyrel J. et al., 2009, A&A, 506, 681
Queyrel J. et al., 2012, A&A, 539, 93
Rieke G. H., Cutri R. M., Black J. H., Kailey W. F., McAlary C. W., Lebofsky M. J., Elston R., 1985, ApJ, 290, 116
Robaina A. R. et al., 2009, ApJ, 704, 324
Robaina A. R., Bell E. F., Wel A. V. D., Somerville R. S., Skelton R. E., McIntosh D. H., Meisenheimer K., Wolf C., 2010, ApJ, 719, 844
Salpeter E. E., 1955, ApJ, 121, 161
Scarlata C. et al., 2007, ApJS, 172, 406
Schruba A. et al., 2011, AJ, 142, 37
Shapiro K. L. et al., 2008, ApJ, 682, 231
Springel V., 2000, MNRAS, 312, 859
Springel V., Yoshida N., White S. D. M., 2001, New Astron., 6, 79
Strateva I. et al., 2001, AJ, 122, 1861
Swinbank A. M., Smail I., Chapman S. C., Blain A. W., Ivison R. J., Keel W. C., 2004, ApJ, 617, 64

Tacconi L. J. et al., 2010, Nat, 463, 781
Teplitz H. I. et al., 2000, ApJ, 542, 18
van Dokkum P. G. et al., 2011, ApJ, 743, L15
Wang Z. et al., 2004, ApJS, 154, 193
Whitaker K. E. et al., 2011, ApJ, 735, 86
Williams R. J., Quadri R. F., Franx M., 2011, ApJ, 738, L25
Wisnioski E., Glazebrook K., Blake C., The WiggleZ Team, 2011a, in Wang W., Lu J., Luo Z., Yang Z., Hua H., Chen Z., eds, ASP Conf. Ser. Vol. 446, Galaxy evolution: Infrared to Millimeter Wavelength Perspective. Astron. Soc. Pac., San Francisco, p. 235
Wisnioski E. et al., 2011b, MNRAS, 417, 2601
Wright S. A., Larkin J. E., Law D. R., Steidel C. C., Shapley A. E., Erb D. K., 2009, ApJ, 699, 421
Wuyts S., Labbé I., Förster Schreiber N. M., Franx M., Rudnick G., Brammer G. B., van Dokkum P. G., 2008, ApJ, 682, 985
Wuyts S. et al., 2012, ApJ, 753, 114
Younger J. D., Hopkins P. F., Cox T. J., Hernquist L., 2008, ApJ, 686, 815

## APPENDIX A: PARAMETRIZATION OF MERGER MORPHOLOGY ($GM_{20}CAS$)

To ease comparison between our visually selected merger candidates and the extensive literature selecting mergers based on empirically determined parametric classification schemes, we have estimated the Gini coefficient ($G$), the second-order moment of the brightest 20 per cent of the light ($M_{20}$), the concentration ($C$), the asymmetry parameter ($A$) and the smoothness parameter ($S$) (e.g. Conselice 2003; Lotz et al. 2004, 2006, 2008b; Papovich et al. 2005; Scarlata et al. 2007; Conselice et al. 2008, 2009) for the objects presented in this paper. We follow Lotz et al. (2008b) when estimating the individual parameters.

In Fig. A1 the estimated $GM_{20}CAS$ parameters are shown for the 60 visually selected 3D-*HST* merger candidates (large black points) and the 292 visually discarded objects (small grey points). The

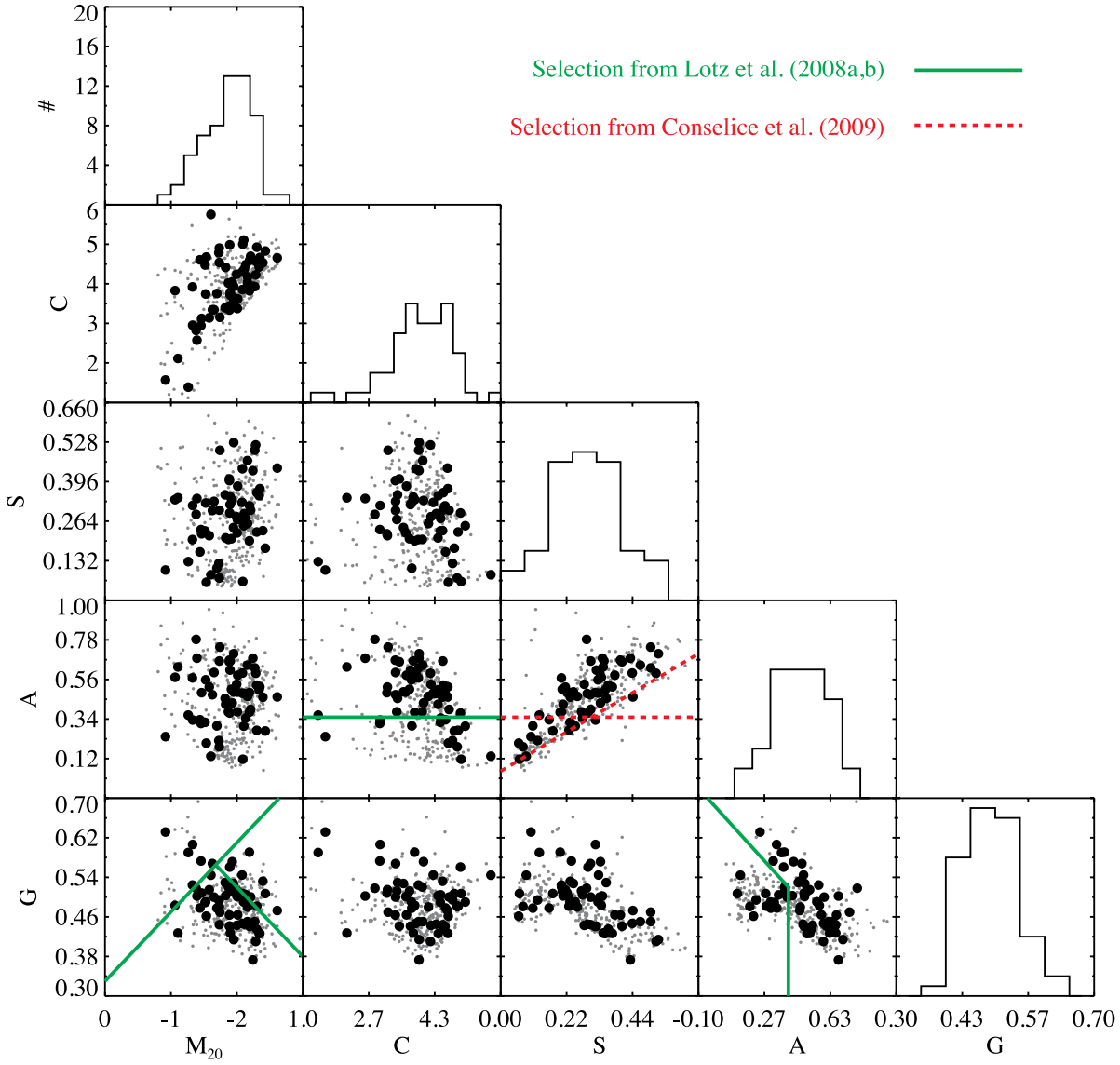


**Figure A1.** The morphological parameters $G$, $M_{20}$, $C$, $A$ and $S$ for the 60 visually selected 3D-*HST* merger candidates (large black points) and the 292 visually discarded objects (small grey points). The histograms show the distribution of the parameters for the 60 merger candidates. The solid green lines in $A$–$C$, $G$–$M_{20}$ and $G$–$A$ space show the suggested merger selection from Lotz et al. (2008a,b). The dashed red lines in $A$–$S$ space are taken from Conselice et al. (2009). Parametrically selected mergers are believed to lie above and/or to the right of the solid and dashed lines.

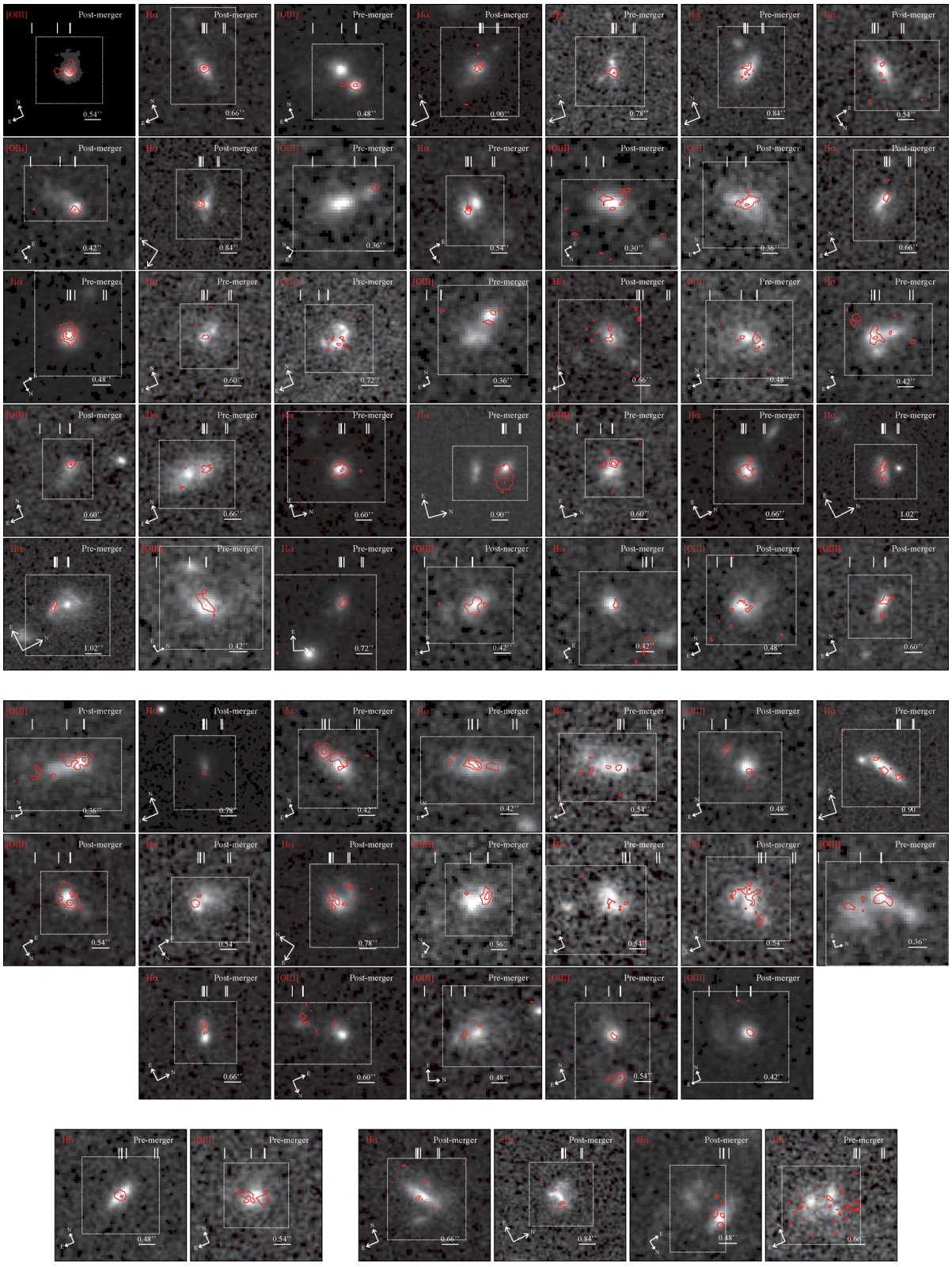

**Figure B1.** Similar to Fig. 5 for the full sample of emission line (star formation) maps obtained from the 60 morphologically selected 3D-*HST* mergers. The maps are sorted according to SF type (Section 5) with the 35 systems of SF type 1 at the top, the 19 SF type 2 systems in the centre and the SF types 3 and 4 mergers, also shown in Fig. 5, at the bottom.

histograms show the distributions of the individual parameters of the 60 merger candidates. The solid green and dashed red lines are from Lotz et al. (2008a,b) and Conselice et al. (2009), respectively. Parametrically selected mergers have been shown to preferentially lie above and to the right of these lines. We see that the majority of the visually selected 3D-*HST* merger candidates indeed have $A > 0.35$ as expected. The $G$–$M_{20}$ selection on the other hand seems to reject the majority of the merger candidates selected here. The selected merger candidates generally trace the parent population and do not distinct themselves clearly as would be expected for a 'clean' merger selection. This is most probably due to the complications that clumpy and irregular morphology of high-$z$ objects and noisy images have on merger selections and in particular on 'blind' parametric classification schemes.

## APPENDIX B: THE 3D-*HST* EMISSION LINE (STAR FORMATION) MAPS

In Fig. B1 we show the full sample of the 60 3D-*HST* emission line (star formation) maps. The objects have been sorted according to the estimated morphology of the star formation (SF type) described in Section 5.

This paper has been typeset from a TEX/LATEX file prepared by the author.